Mon. Not. R. Astron. Soc. **356,** 839–848 (2005) doi:10.1111/j.1365-2966.2004.08519.x

# Very Long Baseline Array imaging of a periodic 12.2-GHz methanol maser flare in G9.62+0.20E

S. Goedhart,[1,2]★ V. Minier,[3] M. J. Gaylard[1] and D. J. van der Walt[2]

[1]*Hartebeesthoek Radio Astronomy Observatory, PO Box 443, Krugersdorp, 1740, South Africa*
[2]*School of Physics, North-West University, Potchefstroom Campus, Private Bag X6001, Potchefstroom, 2520, South Africa*
[3]*Service d'Astrophysique, DAPNIA/DSM/CEA Centre d'Etudes de Saclay, 91 191 Gif-sur-Yvette, France*

Accepted 2004 October 15. Received 2004 October 15; in original form 2004 July 16

**ABSTRACT**

The class II methanol maser source G9.62+0.20E undergoes periodic flares at both 6.7 and 12.2 GHz. The flare starting in 2001 October was observed at seven epochs over three months using the Very Long Baseline Array (VLBA) at 12.2 GHz. High angular resolution images (beam size $\sim$1.7 $\times$ 0.6 mas) were obtained, enabling us to observe changes in 16 individual maser components. It was found that while existing maser spots increased in flux density, no new spots developed and no changes in morphology were observed. This rules out any mechanism which disturbs the masing region itself, implying that the flares are caused by a change in either the seed or pump photon levels. A time delay of one to two weeks was observed between groups of maser features. These delays can be explained by light travel time between maser groups. The regularity of the flares can possibly be explained by a binary system.

**Key words:** masers – stars: formation – ISM: clouds – H II regions – radio lines: ISM.

## 1 INTRODUCTION

Class II methanol masers appear to be closely associated with the earliest evolutionary stages of high-mass stars (Menten 2002; Minier et al. 2003, and references therein). In many cases, the masers at 6.7 or 12.2 GHz are the only indication of star formation activity at a particular site (Walsh et al. 1998; Goedhart, van der Walt & Gaylard 2002). Thus, methanol masers are excellent probes of the changing conditions in the vicinity of young (proto)stars.

The prevalent model for class II methanol masers is the Sobolev–Deguchi model (Sobolev & Deguchi 1994; Sobolev, Cragg & Godfrey 1997). This model has recently been further refined to examine in detail the large number of methanol maser transitions observed in star-forming regions (e.g. Cragg et al. 2001). The model of Sobolev et al. (1997) is the only one which has been able to reproduce the high brightness temperatures ($>10^{12}$ K) observed toward strong methanol maser sources. In this model, the masers arise in a spherically expanding cloud of methanol-rich gas, which is treated under the large velocity gradient (LVG) approximation. The model has approximately 10 free parameters; the most important in terms of producing strong methanol masers are the gas temperature, the dust temperature, the density, the methanol column density and the beaming of the source, which characterizes the elongated maser geometry. Three external sources of continuum are taken into account: the infrared pumping radiation, the cosmic microwave background and possible free–free emission from a H II region. The model requires the temperature of the gas producing the masers to be moderately cool (30 K), with a hydrogen number density in the range of $10^6$ –$10^8$ cm$^{-3}$. In addition, a nearby region of warm (100–200 K) dust is necessary to produce the infrared photons needed to create the population inversion. A dust temperature $>100$ K plays a dual role in producing methanol masers; it is required to release methanol from the dust grains through evaporation and also to pump the methanol molecules to their first and second torsionally excited states. Finally, a methanol column density of $\sim5 \times 10^{17}$ cm$^{-2}$ is needed to account for the observed brightness temperatures.

The region G9.62+0.20 is a high-mass star formation complex with a number of H II regions in different evolutionary stages. Garay et al. (1993) labelled the H II regions A–E in order of increasing compactness. A and B are extended H II regions, C is a bright compact H II region, D is a bright ultracompact (UC) H II region and E has been classified as a hypercompact H II region by Kurtz & Franco (2002). Regions C, D and E are connected by a ridge of dense molecular material with C and D to the north and south of E, respectively (Hofner et al. 1996). A sixth object F, located midway between E and D, was found to have emission from hot, dense molecular dust (Hofner et al. 1996). Recent observations by Testi et al. (2000) found faint thermal radio continuum emission associated with component F. This source is believed to be in the hot molecular core stage and has a high-velocity outflow associated with it (Hofner, Wiesemeyer & Henning 2001).

Sensitive mid-infrared imaging at 11 μm by De Buizer et al. (2003) found three dense cores which matched the positions of H II

★E-mail: sharmila@hartrao.ac.za

regions B, C and E. The mid-infrared emission at G9.62+0.20E is very weak. No near-infrared source was found at this location (Persi et al. 2003).

Franco et al. (2000) calculated the spectral index of G9.62+0.20E from 2.7 mm to 3.5 cm as 0.95 ± 0.06 while Hofner et al. (1996) found a value of 1.1 ± 0.3. Hofner et al. (1996) find this to be consistent with either an ionized stellar wind or a hypercompact H II region (radius <0.0025 pc), with excess dust emission at 2.7 mm and a central star that is probably of spectral type B1.

The observations of Hofner et al. (2001) also found hot methanol at H II region E, but nowhere else in the complex. The most powerful 6.7-GHz methanol maser known is associated with H II region E (Phillips et al. 1998), while a weaker maser is associated with region D. Other maser transitions towards region E include methanol at 12.2 GHz (Caswell et al. 1995), 37.7 GHz (Haschick, Baan & Menten 1989), 85.5 GHz (Cragg et al. 2001) and 107 GHz (Val'tts et al. 1999), hydroxyl at 1665 and 1667 MHz (Caswell 1998), ammonia at 24.5 GHz (Hofner et al. 1994) and water masers in a line between E and F (Hofner & Churchwell 1996). The water masers are probably associated with the outflow from the hot molecular core F. High-resolution observations of the 12.2-GHz methanol masers by Minier, Booth & Conway (2002) show clusters of maser spots in two lines separated by ∼500 au.

A flux density monitoring programme at the Hartebeesthoek Radio Astronomy Observatory (HartRAO) found that the methanol maser in G9.62+0.20E exhibits strong flares recurring with a period of 246 d at both 6.7 and 12.2 GHz (Goedhart, Gaylard & van der Walt 2003, 2004). This is the first reported incidence of periodic variations associated with a high-mass star formation region. The likely mechanism is strongly constrained by the period observed. High-mass stars on the main sequence can undergo $\beta$ Cephei pulsations, but these periods are between 0.1 and 0.6 d. Examination of the classes in the General Catalogue of Variable Stars (Kholopov et al. 1985) shows that the only pulsating stars with the appropriate periods are Miras. These are evolved stars and therefore unlikely to be the cause of the variations. The rotational velocities of main-sequence O- and B-type stars are typically of the order of 400 km s$^{-1}$ (Lang 1992), which gives rotational periods between 0.5 and 2 d. A recent study of pre-main-sequence periodicity in an OB association found rotational periods ranging from less than a day up to 28 d (Makidon et al. 2004). Again, these periods are far too short to be related to the variations in the masers.

The young star FU Orionis is the prototype of a class of young stellar objects that experience episodic outbursts due to high disc accretion rates and instabilities in the disc accretion. The duration of these outbursts is of the order of decades and the interval between outbursts is believed to be thousands of years (Kenyon et al. 2000, and references therein). The time-scales involved here are far too great to present a feasible explanation of the methanol maser flares.

The periodic variations could be modulated by a disc–outflow system. The numerical simulations of Yorke & Sonnhalter (2002) have shown that massive stars can form from disc accretion collapse of molecular cloud clumps. The simulations of Durisen et al. (2001), Yorke & Sonnhalter (2002) and Ouyed, Clarke & Pudritz (2003) have shown that the accretion disc develops a rotating spiral density pattern. On the other hand, the outflows themselves could cause variations with the appropriate periods; Ouyed et al. (2003) found that the outflow jets can develop a corkscrew structure or a wobbling motion. The rotation rate of the corkscrew is dependent on its distance from the origin, with the minimum rotation rate at approximately 85 d for a B0 star. G9.62+0.20E is not directly associated with an outflow, although the core at region F does have an outflow.

Another possibility is that the central star is a binary system. More than 50 per cent of optically visible stars of types O9 to M appear to have companions (Abt 1979, 1983; Halbwachs 1983). Poveda, Allen & Parrao (1982) have shown that the incidence of binary and multiple systems may be closer to 100 per cent once observational limitations have been taken into account. A recent study of the multiplicity in Herbig–Haro sources gives a binary frequency between 79 and 86 per cent, with half of the systems being higher-order multiples (Reipurth 2000). Simulations of accretion and collisions in stellar clusters (Bonnell & Bate 2002) indicate that binary systems can form through three-body interactions. In addition, it is known that high-mass stars tend to form in clusters (Clarke, Bonnell & Hillenbrand 2000). Therefore, there is a strong possibility that the central star exciting the masers could have a companion. Assuming a 11-$M_{\odot}$ star (B1) with a less massive companion, the orbital radius of the companion would be 1.7 au to give a period of 246 d.

Thus, the presence of periodic variations in these masers could lead to important insights into the high-mass star formation process.

Single-dish monitoring at HartRAO shows that time delays occur in the flaring of different maser features (Goedhart et al. 2003), but the velocity overlap of some of the maser spots means that the spectral line observations cannot give us much information on the spatial propagation of the flare. Imaging of the masers during a flare would define the projected spatial sequence of the flaring and thus help to identify the mechanism causing the flare, or eliminate some possibilities. Because this source is reasonably strong at 12.2 GHz and the flares are even more pronounced than at 6.7 GHz, the Very Long Baseline Array (VLBA), with its 12-GHz capability, was judged to be the ideal instrument for imaging the maser components. Seven observations were carried out during the period of 2001 October to December.

The observations and reduction method are described in Section 2. The results are presented in Section 3 and discussed in Section 4. The conclusions are presented in Section 5.

## 2 OBSERVATIONS AND REDUCTION

The observation dates were selected such that the various phases of the flare could be covered effectively. There is a period of about two weeks during which the main peak of the maser slowly increases in intensity. It was judged that one observation would be sufficient during this period. The maser then rapidly increases in intensity over the next two weeks and remains at its peak for less than a week before starting to decay. Four observations at weekly intervals were requested during this stage. The decay phase takes another two months, but just two more observations at two-week intervals were used.

Table 1 gives the dates of the observing runs, along with an estimate of the rate of the flare from the folded time-series of several cycles. Fig. 1 shows the timing of the observations relative to the flare cycles. The progress of the flare during this time was closely monitored at HartRAO (as described in Goedhart et al. 2003) in order to ensure that the VLBA observations were correctly timed.

The observations, at both left and right circular polarizations, were carried out using the full VLBA at 2 cm. The continuum source J1733−1304 was used as a calibrator. The sequence of scans consisted of 5 min on the calibrator and 30 min on-source. The total observing time per session, including the calibration observations, was 6 h. Because the maser features span ∼10 km s$^{-1}$, a

**Table 1.** Timing of the VLBA observations.

| Observation | Date (yyyy-mm-dd) | Day of cycle | Rate of flare (Jy h$^{-1}$) |
|---|---|---|---|
| I | 2001-10-11 | 14 | 0.19 |
| II | 2001-10-18 | 21 | 0.13 |
| III | 2001-10-22 | 25 | 0.07 |
| IV | 2001-10-30 | 33 | 0.06 |
| V | 2001-11-07 | 41 | 0.14 |
| VI | 2001-11-21 | 55 | 0.06 |
| VII | 2001-12-09 | 73 | 0.01 |

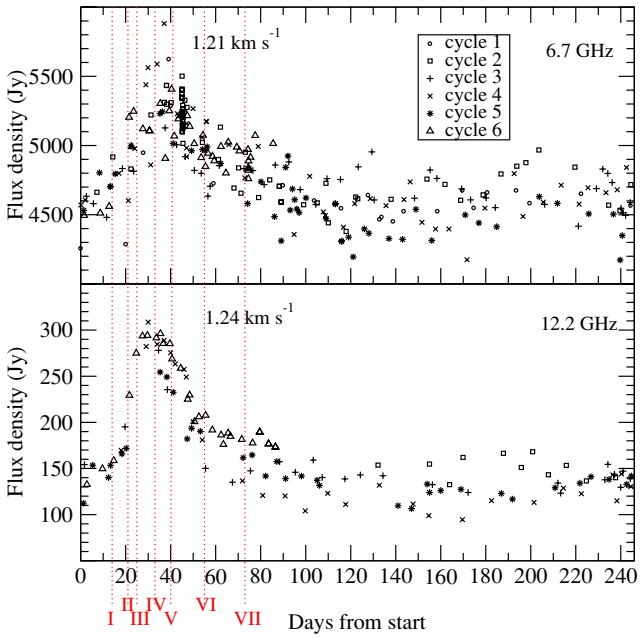


**Figure 1.** Timing of the VLBA observations relative to the flare cycle of feature C in G9.62+0.20E. The dotted lines indicate the times of the VLBA observations during cycle 5.

bandwidth of 1 MHz (covering 25 km s$^{-1}$) was used. The observations were correlated at the VLBA correlator in Soccoro (USA) using 512 channels, giving a velocity resolution of 0.05 km s$^{-1}$. The central velocity (at channel 257) was 1.28 km s$^{-1}$ and a rest frequency of 12 178.595 MHz was adopted.

The data were calibrated and reduced using standard procedures in the Astronomical Image Processing System (AIPS).

Correlator digitization errors were corrected using the task ACCOR. The data were examined for bad scans and flagged using SPFLAG and IBLED. The fringe rate for the continuum calibrator was found using FRING, before using BPASS to find the time-dependent bandpass corrections for both the autocorrelated and cross-correlated spectra. The velocity information for the source was entered into the catalogues using SETJY. The Doppler changes in velocity were corrected using CVEL. This task also applies the bandpass calibrations to the data.

There are two options for the amplitude calibration. The first is to use an external continuum calibrator observed at regular intervals. This has the disadvantage of requiring more observing time off the source of interest. The other option is to select a total-power spectrum from a reliable antenna as a template spectrum, and to use the gain calibration for that antenna. We adopted this method and assumed that the amplitude of the maser remained constant during the 6 h of the observation. The maximum rate of change in the intensity of the dominant maser feature is 0.2 Jy h$^{-1}$, which gives a change of 1.2 Jy, at most, over 6 h. The template spectrum had to have no bad data in it and be taken at maximum elevation. The most important criterion was to make sure that there were no signs of radio frequency interference during the scan because this leads to errors in the recorded system temperature. The system temperatures for the scan were examined carefully to make sure that a constant value was recorded. Once a suitable template spectrum was found, it was compared to all the scans at each antenna and a gain correction calculated relative to it, using the task ACFIT. The ACFIT solution was examined and note was taken of solutions with extremely high gain, indicating high attenuation of the signal, usually due to dense cloud, rain or the source being low on the horizon. Once the amplitude calibration was applied, the data with high gain corrections were flagged using IBLED.

The time-dependent phase delay, or instrumental delay, was found by running FRING on the continuum calibrator. The delay solution was smoothed using SNSMO and then applied to the maser source using two-point interpolation.

The phase rate calibration was found using a compact maser feature as the source model in FRING. The channel used corresponded to a feature at 3.6 km s$^{-1}$ and was visible in the cross-power spectra for the longest baselines, indicating that it is a very compact source. The solutions were examined to make sure they did not have any abrupt changes, which would indicate the solution interval was too long. A solution interval of 0.5 min was used, while the time interval in the calibration table (CL table) was 0.1 min.

The quality of the image can be improved by performing self-calibration to remove the effects of rapidly changing atmospheric conditions, which have not been removed in the previous calibration steps. Because the science goal involved tracking changes in maser amplitude, it was important to retain the absolute amplitude calibration. Hence, no further amplitude calibrations were carried out, because self-calibration, while it improves the signal-to-noise (S/N), destroys the absolute amplitude calibration. The self-calibration on the phase was performed by using a compact maser spot as a reference channel. A preliminary image using 100 CLEAN components from IMAGR was used as the source model, which was then input back into CALIB. The subsequent solution was applied to the reference channel and a new image and source model was generated by IMAGR. The procedure was iterated until the solution converged. The images were checked at each stage to ensure there was indeed an improvement in the image quality. The rms noise of the images was checked using IMSTAT. The solutions typically converged after five iterations. The derived corrections were then applied to all the other channels. The final data cube was produced using IMAGR with a cell size of 0.2 mas. The data were CLEANed until the residual flux limit was 60 mJy (about four times the theoretical rms noise). This self-calibration method destroys the absolute position information; hence, all maps displayed in this paper are relative to the reference feature. The nominal position of this feature is at RA 18:06:14.655, Dec. −20:31:31.60 (J2000), using the observations of Minier et al. (2002) as a reference for the map centre.

Care was taken in the identification of maser components on the final image because errors in the calibration or imaging process may lead to artefacts. Phase errors can cause multiple identical features scattered around the correct position. The phase calibration was repeated and data with bad solutions were flagged out until no such artefacts were seen in the images. Imperfect subtraction of the dirty beam's sidelobes can create features resembling the sidelobes. The sidelobe artefacts have an amplitude of the order of 0.5 per cent of

the peak flux density of the maser spot, so they are not dominant in the images.

## 3 RESULTS

### 3.1 Structure of the maser components

The data cubes were examined using the KARMA (Gooch 1997) data visualization tools KRENZO, KVIS and XRAY. Of the 512 velocity channels, only the central 158 channels contain the maser emission. The rest of the channels were disregarded in the analysis. 16 individual maser components having distinct spatial positions and velocity ranges were identified. Zero-moment maps, in which the data cube is integrated along the velocity axis for specific velocity ranges, were made using KRENZO. The images of Minier et al. (2002) show the same overall structure as seen here, but the longer integration times used here (6 h compared to about 1 h) give a better *uv*-coverage, with the result that feature E is resolved into five separate, compact components. Table 2 gives the selected velocity ranges for the components and Fig. 2 shows their spatial distribution. The nomenclature of Minier et al. (2002) is adopted and expanded on where necessary.

**Table 2.** Velocity ranges of 12.2-GHz maser components in G9.62+0.20E.

| Label | Start velocity (km s$^{-1}$) | End velocity (km s$^{-1}$) |
|---|---|---|
| E3 | 4.068 | 4.357 |
| E4 | 4.068 | 4.357 |
| E1 | 3.444 | 4.021 |
| E2 | 2.722 | 3.396 |
| E5 | 2.722 | 3.396 |
| D | 2.049 | 2.674 |
| A | 1.713 | 2.001 |
| B | 1.328 | 1.664 |
| C1 | 0.991 | 1.424 |
| C2 | 0.991 | 1.424 |
| F1 | −0.499 | 0.222 |
| I | −0.499 | −0.162 |
| G1 | −1.316 | −0.547 |
| G2 | −1.028 | −0.547 |
| H | −2.181 | −1.364 |
| F2 | −2.999 | −2.230 |

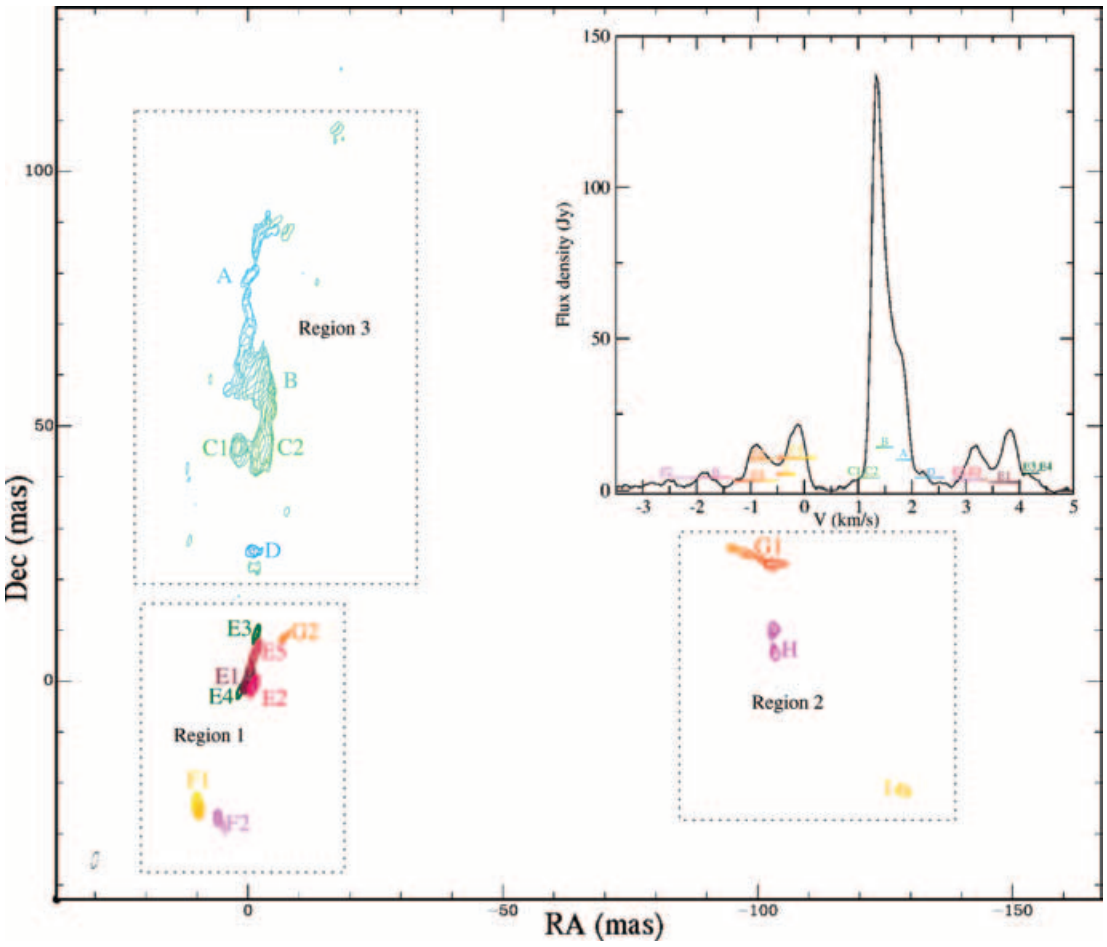


**Figure 2.** Distribution of maser features in G9.62+0.20E. The figure was taken from the fourth VLBA observation, when features A, B, C and D were at their maximum intensity. The features are colour-coded according to velocity. The contour levels are at 0.2 Jy beam$^{-1}$ in each velocity channel. The inset shows the 12.2-GHz total power spectrum. The colour bars superimposed on the spectrum indicate the corresponding colour range in the contour map and the features are labelled on the contour map and on the spectrum. Some spurious features due to the sidelobes of the beam can be seen at the same velocity as features C1 and C2. The restoring beam is shown to the bottom left.

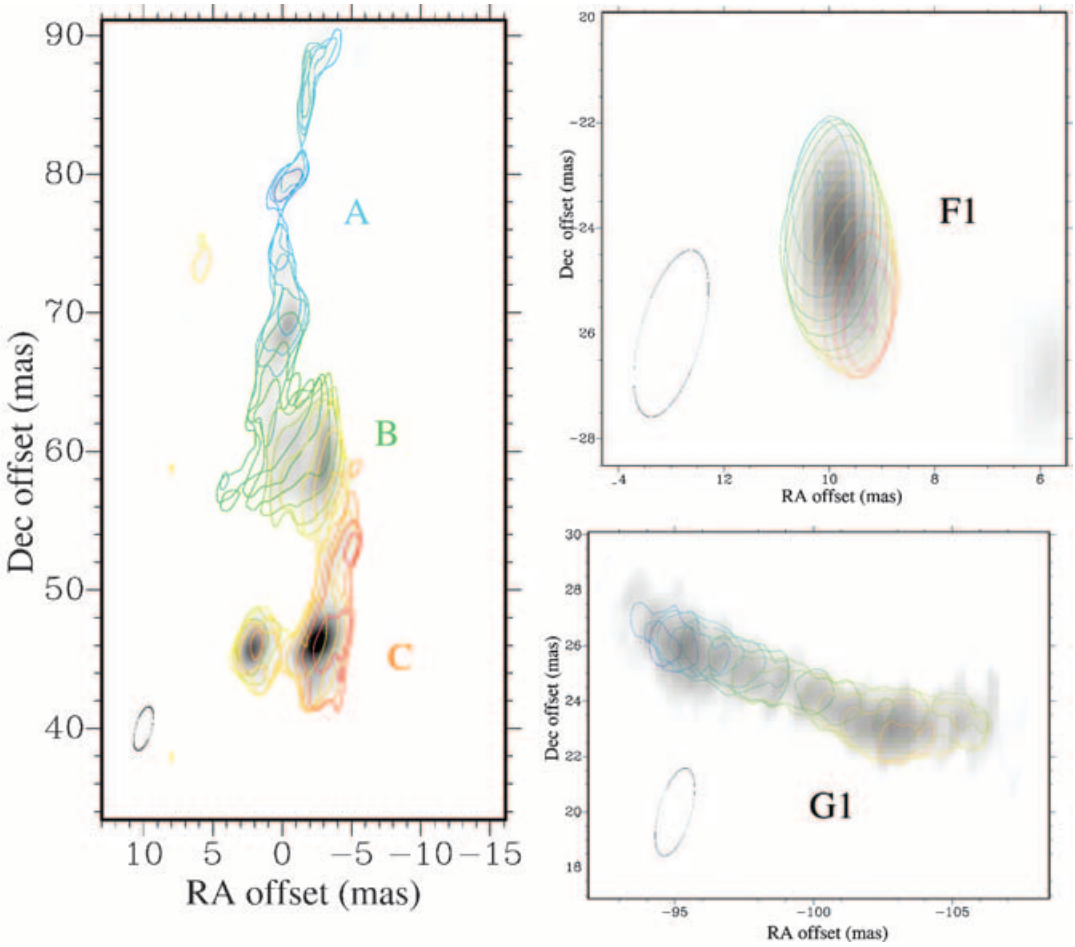


**Figure 3.** Close-up images of the velocity structure of various maser components. Each colour contour corresponds to a different velocity channel, with the contour limit at 0.2 Jy beam$^{-1}$. The complex of components A, B and C is shown in the left-hand panel. Component F1 is shown to the upper right and G1 to the bottom left.

The maser components A, B and C are connected by weaker emission. Minier et al. (2002) speculated that component D may be linked to components A, B and C by diffuse emission, but no evidence of such emission is seen here. Region E has a complex structure, with five distinct compact maser components. A channel from the component E2 was used as the reference channel for the phase calibration because of its compactness. G1 has a linear structure with a strong velocity gradient. H consists of two smaller components connected by slightly weaker emission, but it has been treated as one structure in the following analysis. D and I are weak but compact spots.

The maser components appear to have velocity gradients. This can be seen most clearly in the transition from features A–C, and in F1 and G1 (Fig. 3). The velocity gradient in the group of components A–C is $\sim$0.004 km s$^{-1}$ mas$^{-1}$, while it is 0.20 and 0.22 km s$^{-1}$ mas$^{-1}$ in components F1 and G1, respectively. Assuming that the distance to G9.62+0.20 is 5.7 kpc (Hofner & Churchwell 1996), the velocity gradient for F1 and G1 is $\sim$0.03 km s$^{-1}$ au$^{-1}$.

Different baselines act as filters for different scales of structures. It is possible that some flux could be resolved out for the features with large-scale structures because there is no information from extremely short baselines. The amount of flux that is resolved out in the cross-power spectra has to be checked as this could affect the interpretation of the variability in the images. The top panel in Fig. 4 shows a total power spectrum, which is equivalent to a single-dish spectrum, at the Los Alamos antenna and a cross-power spectrum between Los Alamos and Pie Town, the shortest baseline in the VLBA. Most of the flux for feature F2 has been resolved out, while there is considerable flux loss for features H, G, I, F1 and D. There is moderate flux loss on features A, B and C while features E1–E5 do not appear to have significant diffuse emission. The second panel shows a cross-power spectrum between Brewster and Mauna Kea, in which the dominant maser feature at 1.2 km s$^{-1}$ is mostly resolved out, while the more compact features at 3 and 4 km s$^{-1}$ (features E1–E5) are still clearly visible. The third panel shows the longest baseline, between St Croix and Mauna Kea, where only the most compact features are visible in the spectrum. It can be seen that features A, C, D and G have compact components. Therefore, these observations will not provide information on the behaviour of the entire maser region. However, as will be discussed in the next section, the flare is still observed with the full VLBA. We assume, on this basis, that the behaviour of the compact cores can be taken as being representative of what is happening to any particular feature but it will not be possible to do any in-depth quantitative analysis such as estimating the increase in the pump or seed photons.

Another way of examining the structure is with visibility amplitude versus *uv*-distance plots, which show the amount of emission seen at the different scales. Fig. 5 shows the visibility amplitudes versus *uv*-distance of the channels corresponding to each spectral

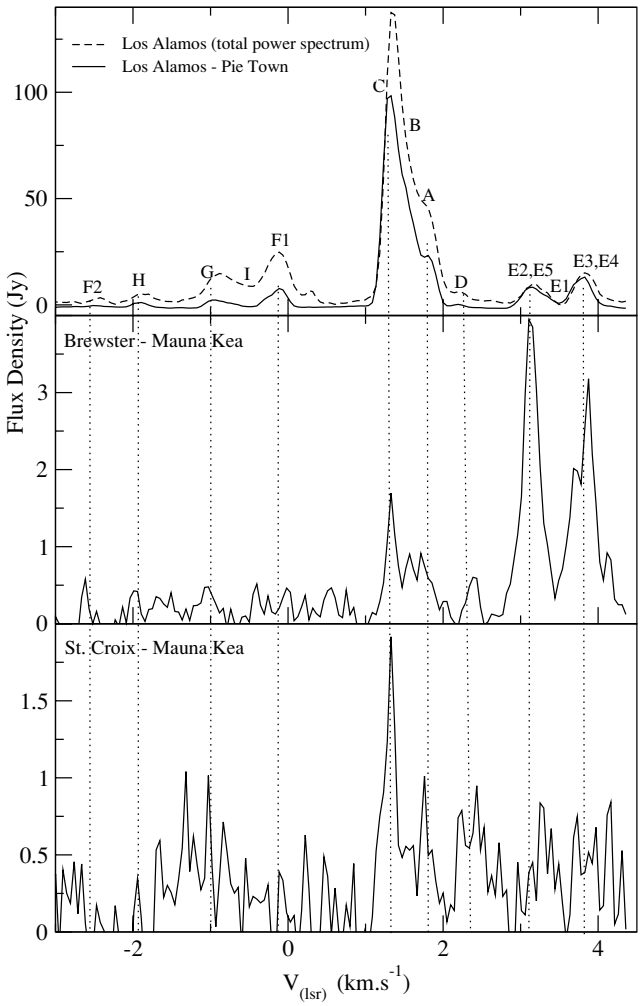


**Figure 4.** Examples of total power (top panel) and cross-power spectra.

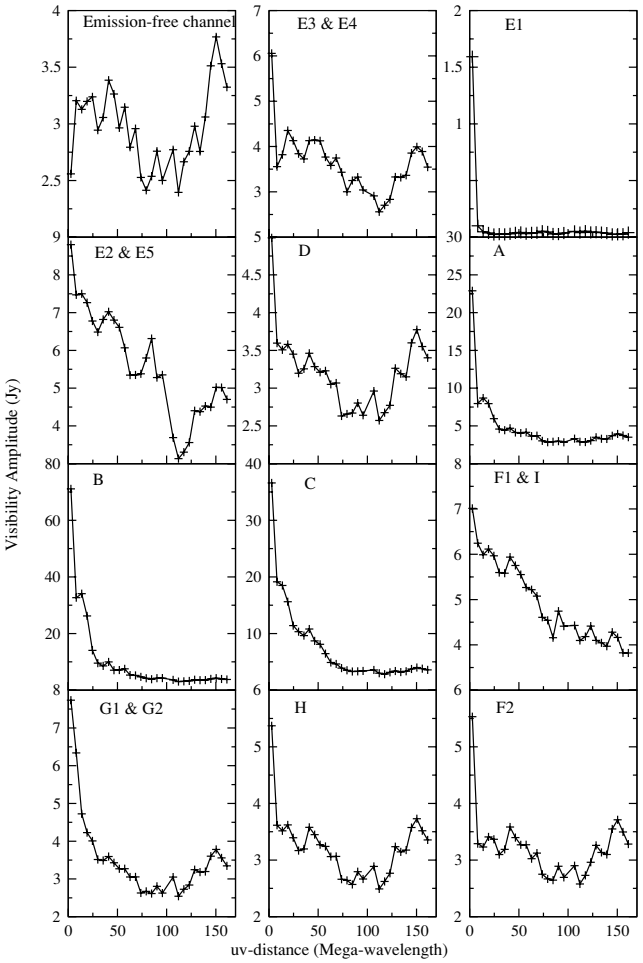


**Figure 5.** Visibility versus *uv*-distance for the maser features. The visibility amplitudes have been averaged and binned.

feature. The top-left panel shows an emission-free channel as an estimate of the noise. The noise will be reduced as the square root of the number of channels averaged for each feature. The longer *uv*-distances show the smaller-scale structures. Thus, greater emission at smaller *uv*-distance and a rapid drop to zero in amplitude towards greater *uv*-distance indicates a source that has predominantly large-scale structure and is 'resolved out' on the longest baselines. It can be seen that the emission from features A, B, C and E1 comes predominantly from large-scale structures, but they do have compact cores visible at the longest baselines. The emission does not drop to the noise level for features A, B and C, implying that they may have compact cores which are not fully resolved. The emission at longer baselines drops to the noise level for features D, G1, G2, H and F2; hence, they are fully resolved at the longest baselines. These results are consistent with those of Minier et al. (2002). The other features have the same velocities so it is not possible to extract the information about their structure from the amplitude versus *uv*-distance plots.

### 3.2 Variations during the flare

The antennas at Pie Town, Hancock and Fort Davis were either unavailable, or data from them were not usable because of bad weather during some of the observations. As a result of this, the beam sizes for the different epochs are not consistent if all available antennas for a particular observation are used. This affects the observed flux density and apparent structure of the masers. Therefore, these antennas were flagged out of all the data sets before running IMAGR to produce the data sets for the following analysis. The resulting beam parameters are listed in Table 3. There are still some small variations in beam size and orientation because of temporary problems with some antennas, but these should have only a minor effect on the following calculations.

**Table 3.** Beam parameters for the different epochs with Pie Town, Hancock and Fort Davis flagged out for all epochs.

| Epoch | Major axis (mas) | Minor axis (mas) | Position angle (°) |
|---|---|---|---|
| I | 1.7 | 0.59 | −16.27 |
| II | 1.8 | 0.62 | −21.04 |
| III | 1.7 | 0.56 | −6.86 |
| IV | 1.7 | 0.56 | −14.64 |
| V | 1.7 | 0.60 | −14.45 |
| VI | 1.7 | 0.69 | −20.79 |
| VII | 1.7 | 0.72 | −21.90 |

Imaging of individual channels results in a 'data cube' with an image of each channel. Zero-moment maps were created by averaging across all the velocity channels in order to produce a single image. The zero-moment maps for each epoch, derived from the full

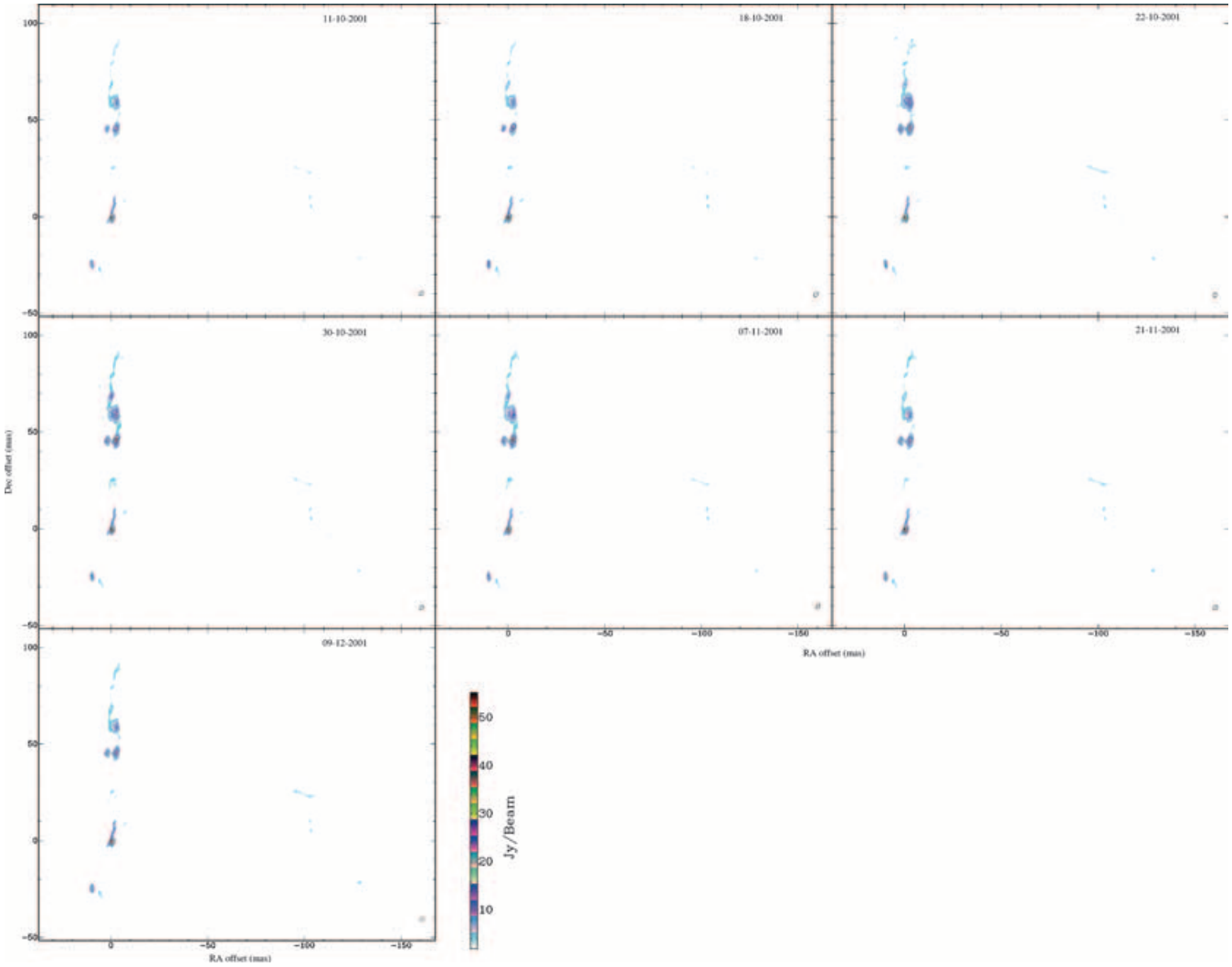


**Figure 6.** Zero-moment images for each epoch. The restoring beam is shown to the bottom right in each panel. An animated version of this flare sequence will be available on-line at http://www.blackwellpublishing.com/products/journals/suppmat/MNR/MNR8519/MNR8519sm.htm.

velocity range in which emission is present, are shown in Fig. 6.[1] There appear to be no changes in the morphology of the maser components during the flare. The proper motion studies of Minier et al. (2001) indicate that the greatest proper motion in this source is of the order of 0.7 mas yr$^{-1}$ and, indeed, no motion of the maser features relative to the phase centre, to within 0.2 mas, was seen during the two months of the monitoring campaign. In addition, no new maser spots are formed during the flare. The maser components simply become brighter and then start to fade to their pre-flare intensity.

Time series were found for each maser feature using the task BLSUM in the following manner. Zero-moment maps were constructed for each of the velocity ranges given in Table 2. The noise levels for each map were estimated using IMSTAT on an emission-free region of the image (the top right-hand corner does not have emission at any velocity). The noise pixels were then set to an INDEF value using BLANK. BLSUM requires a template blotch map, which is used to manually select the area over which to sum. The blotch templates were constructed by averaging the noise-blanked maps for all the epochs using SUMIM. The input data cube for BLSUM consisted of the zero-moment maps for each epoch, so that the third axis of the cube was in fact a time axis. BLSUM cannot automatically correct for the beam size in such a situation, so the flux density is given as an average brightness in Jy beam$^{-1}$. An absolute flux density, which is independent of the beam size, can be calculated by finding the beam size in pixel beam$^{-1}$ for each epoch, converting the average brightness to units of Jy pixel$^{-1}$ and then multiplying by the total number of pixels in the blotch image.

The results of the calculations are shown in Fig. 7. The error bars indicate the rms noise found in each image. The HartRAO time-series of single spectral channels at the peaks of features B and C are shown in the top panel. The maser features A, B, C and D appear to follow the same trend as seen at HartRAO, providing an independent confirmation of the amplitude calibration of the VLBA data. There appear to be three different trends in the time-series, depending on the positions of the masers. The masers have been grouped into three different regions based on this behaviour. The progress of the flare is best sampled amongst the features A, B, C and D. The flare appears to peak earlier at the other two groups. The exact times of the peak of the flares at the different maser components cannot be

[1] A high-resolution animated image will be made available on-line at http://www.blackwellpublishing.com/products/journals/suppmat/MNR/MNR8519/MNR8519sm.htm.

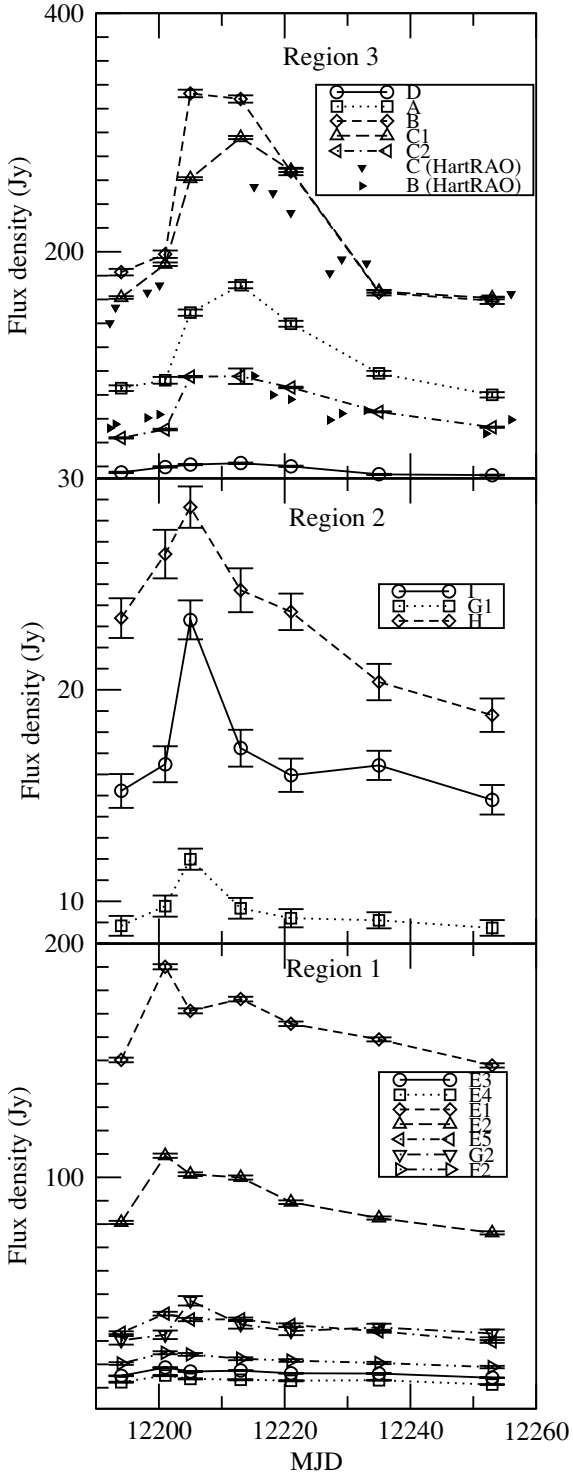


**Figure 7.** VLBA time-series for maser features in G9.62+0.20E. The three panels are divided according to the spatial distribution of the masers. The single-dish observations at HartRAO are also shown for features C and B.

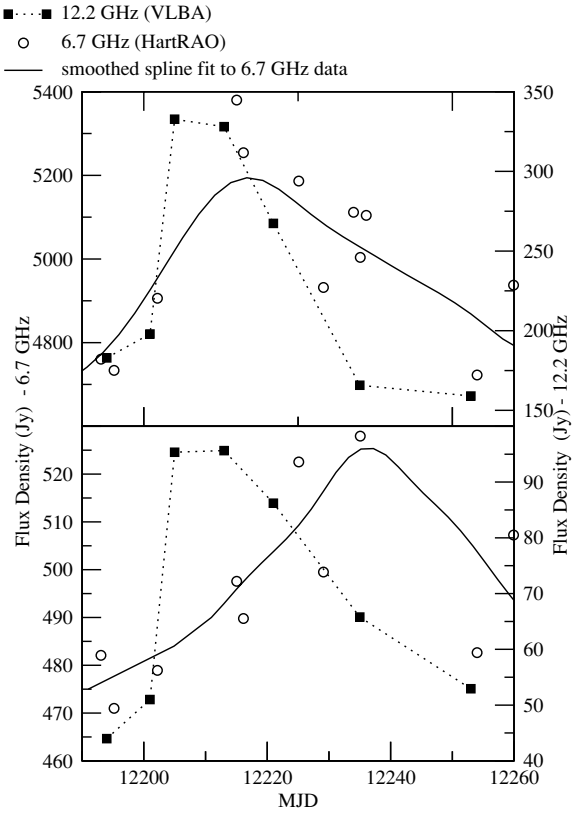


**Figure 8.** Comparison of flux density at 12.2 and 6.7 GHz for the 1.21 km s$^{-1}$ feature (top panel) and the $-0.14$ km s$^{-1}$ feature (bottom panel). Smoothed spline curves (solid lines) were generated for the noisy 6.7-GHz data.

determined because of the poor time resolution, but there may be a one to two week delay in the propagation of the flare through the different regions.

The flare reached its maximum between epochs I and III in region 1, while the maximum could be anywhere between epochs II and IV in region 2. There is a gap in the observations at HartRAO due to bad weather, but from comparison with other cycles it is likely that the flare in region 3 peaked a few days before epoch IV. Unfortunately, the S/N of the 12.2-GHz HartRAO observations of the weaker spectral features was inadequate to permit an analysis of their time-series.

The maser feature at 1.21 km s$^{-1}$ flares simultaneously at both frequencies but the $-0.14$ km s$^{-1}$ feature (F1) at 12.2 GHz appears to flare approximately 30 d before the same feature at 6.7 GHz (Fig. 8). The disparity in the apparent times of the flares may possibly be explained if the 6.7-GHz maser spot is not in the same spatial region as the 12.2-GHz maser or because the pumping conditions in the two transitions are not identical. This issue cannot be explored any further until high-resolution spot maps at 6.7 GHz are obtained and observations with better time resolution are obtained for the 12.2-GHz flares.

## 4 DISCUSSION

### 4.1 Possible flare mechanisms

The lack of change in the structure of the masers themselves, and the fact that the masers return to almost the same pre-flare level after each flare, strongly suggests that the cause of the flare is external to the masing region. This rules out the possibility of a disturbance such as a shock wave or a clump of matter actually passing through the masing region, because this would radically change the structure of the maser components. Two plausible possibilities are an increase in the seed photons or, assuming that the masers are radiatively

pumped, an increase in the pumping radiation. This could be caused by stellar pulsations or periodic outbursts, or by a binary system.

If variations in the seed photons are causing the variability, the cause of the modulation would probably be intrinsic to the star because the cloud is optically thin to radiation at 6.7 and 12.2 GHz. However, as discussed in Section 1, there is no known stellar pulsation mechanism that could cause variations on the time-scales observed. A possible means of causing periodic outbursts in the star may be repeated mass dumps from the accretion disc, similar to those seen in cataclysmic variables. This would still require a mechanism to modulate the accretion flow rate in a periodic manner.

A close binary system seems to be the most plausible mechanism because of the well-defined periodicity of the flares and the small orbital radius implied by the period. As the flares last for three months, the modulation cannot be a simple effect, because the angular size of the stars would be too small to give rise to an effect that lasts for a third of the orbital period. It is more likely that the effect is due to the motion of a large condensation. It should be possible, with detailed modelling, to determine some of the characteristics of this structure because the flares are asymmetric in this source, showing a rapid rise and slow decay. Binary systems in the earliest stages of stellar evolution have not been studied at all in the case of high-mass stars, but the same sort of dynamics found in low-mass systems would probably apply. The environment of a young binary system can be highly complex, with interacting circumstellar discs around each star, as well as a circumbinary disc around the entire system (Lubow & Artymowicz 2000, and references therein). In addition to this, there is the surrounding molecular cloud, with possible accretion flows on to the discs. The interaction of all of these elements may cause strong modulations of the infrared radiation reaching the maser regions. The effects of the propagation of radiation in a region with such complex morphology cannot be easily predicted. The optical depth of the dust is wavelength-dependent and different optical depths will shift the radiation to different wavelengths. It is not clear whether an enhancement of the radiation from the central star(s) would lead to a maser flare, or if an eclipse would shift the wavelength of the radiation reaching the maser regions to the appropriate wavelength for maser pumping. This problem can only be solved by modelling the radiative transfer in different scenarios.

### 4.2 Time delays in the flare

The delay in the peak of the flares may possibly be explained from an analysis of light travel times. The projected sizes of the different regions are as follows. The longest extent of region 1 is ∼44 mas, which at an assumed distance of 5.7 kpc gives 247 au. The light travel time across this distance is 1.3 d. The longest extent of region 2 is ∼63 mas or 357 au, which gives a light travel time of 1.9 d. The longest extent of region 3 is ∼67 mas or 384 au, which gives a light travel time of 2.3 d. Because the interval between observations with the VLBA is of the order of a week, delays of about a day would not be detected.

The projected distances between the regions are as follows. The separation between regions 1 and 2 is approximately 665 au or 3.6 d, between regions 1 and 3 approximately 437 au or 2.4 d, and between regions 2 and 3 760 au or 4.2 d. The observed time delays are of the order of a week or more. The discrepancy could be explained if the maser groups are not at the same distance along the line of sight. Another possibility is if the modulating radiation is strongly beamed and moves across the sky in such a way as to pass across each region in succession. However, it is not obvious how such an effect or the observed pattern would be created.

## 5 CONCLUSION

The series of images taken over the course of three months show no change to the structure or relative positions of the maser components. The mechanism causing the flare is therefore spatially separate from the masers. The flares are probably caused by modulation of the pumping infrared radiation. The regularity of the flares is best explained by a binary system.

The evidence of a delay in the propagation of the flare in different maser components is worth further investigation because this may help locate the origin of the cause of the flares, or be a means of estimating the relative offset of the maser groups along the line of sight.

## ACKNOWLEDGMENTS

The authors would like to thank Mark Claussen at the National Radio Astronomy Observatories (NRAO) for making sure that the observations were correctly scheduled and for preparing the SCHED file. The authors would also like to thank Athol Kemball for his extensive advice on amplitude calibration of spectral-line very long baseline interferometry data.

## REFERENCES

Abt H. A., 1979, AJ, 84, 1591
Abt H. A., 1983, ARA&A, 21, 343
Bonnell I. A., Bate M. R., 2002, MNRAS, 336, 659
Caswell J. L., 1998, MNRAS, 297, 215
Caswell J. L., Vaile R. A., Ellingsen S. P., Norris R. P., 1995, MNRAS, 274, 1126
Clarke C. J., Bonnell I. A., Hillenbrand L. A., 2000, in Mannings V., Boss A., Russell S. S., eds, Protostars and Planets IV. The Formation of Stellar Clusters. University of Arizona Press, Tuscon, p. 151
Cragg D. M., Sobolev A. M., Ellingsen S. P., Caswell J. L., Godfrey P. D., Salii S. V., Dodson R. G., 2001, MNRAS, 323, 939
De Buizer J. M., Radomski J. T., Telesco C. M., Piña R. K., 2003, ApJ, 598, 1127
Durisen R. H., Mejia A. C., Pickett B. K., Hartquist T. W., 2001, ApJ, 563, L157
Franco J., Kurtz S., Hofner P., Testi L., García-Segura G., Martos M., 2000, ApJ, 542, L143
Garay G., Rodriguez L. F., Moran J. M., Churchwell E., 1993, ApJ, 418, 368
Goedhart S., van der Walt D. J., Gaylard M. J., 2002, MNRAS, 335, 125
Goedhart S., Gaylard M. J., van der Walt D. J., 2003, MNRAS, 339, L33
Goedhart S., Gaylard M. J., van der Walt D. J., 2004, MNRAS, 355, 553
Gooch R. E., 1997, PASA, 14, 106
Halbwachs J. L., 1983, A&A, 128, 399
Haschick A. D., Baan W. A., Menten K. M., 1989, ApJ, 346, 330
Hofner P., Churchwell E., 1996, A&AS, 120, 283
Hofner P., Kurtz S., Churchwell E., Walmsley C. M., Cesaroni R., 1994, ApJ, 429, L85
Hofner P., Kurtz S., Churchwell E., Walmsley C. M., Cesaroni R., 1996, ApJ, 460, 359
Hofner P., Wiesemeyer H., Henning T., 2001, ApJ, 549, 425
Kenyon S. J., Kolotilov E. A., Ibragimov M. A., Mattei J. A., 2000, ApJ, 531, 1028
Kholopov P. N. et al., 1985, General Catalogue of Variable Stars, 4th edn. Nauka Publishing House, Moscow
Kurtz S., Franco J., 2002, in Henney W. J., Franco J., Martos M., Peña M., eds, Rev. Mex. Astron. Astrofis. Conf. Ser. Vol. 12, Ionized Gaseous Nebulae. UNAM, Mexico, p. 16
Lang K. R., 1992, Astrophysical Data: Planets and Stars. Springer-Verlag, Berlin

Lubow S. H., Artymowicz P., 2000, in Mannings V., Boss A., Russell S. S., eds, Protostars and Planets IV. Interactions of Young Binaries with Discs. University of Arizona Press, Tuscon, p. 731
Makidon R. B., Rebull L. M., Strom S. E., Adams M. T., Patten B. M., 2004, AJ, 127, 2228
Menten K. M., 2002, in Migenes V., Reid M., eds, IAU Symp. 206, Cosmic Masers: From Protostars to Black Holes. Interstellar Methanol Masers. Astron. Soc. Pac., San Francisco, p. 125
Minier V., Booth R. S., Ellingsen S. P., Conway J. E., Pestalozzi M. R., 2001, in Conway J. E., Polatidis A. G., Booth R. S., Pihlstroem Y., eds, Proc. 5th European VLBI Network Symp., Methanol Masers: Tracers of Outflows? Chalmers Univ. of Technology, Gothenburg, p. 178
Minier V., Booth R. S., Conway J. E., 2002, A&A, 383, 614
Minier V., Ellingsen S. P., Norris R. P., Booth R. S., 2003, A&A, 403, 1095
Ouyed R., Clarke D. A., Pudritz R. E., 2003, ApJ, 582, 292
Persi P., Tapia M., Roth M., Marenzi A. R., Testi L., Vanzi L., 2003, A&A, 397, 227
Phillips C. J., Norris R. P., Ellingsen S. P., McCulloch P. M., 1998, MNRAS, 300, 1131
Poveda A., Allen C., Parrao L., 1982, ApJ, 258, 589
Reipurth B., 2000, AJ, 120, 3177
Sobolev A. M., Deguchi S., 1994, A&A, 291, 569
Sobolev A. M., Cragg D. M., Godfrey P. D., 1997, A&A, 324, 211
Testi L., Hofner P., Kurtz S., Rupen M., 2000, A&A, 359, L5
Val'tts I. E., Ellingsen S. P., Slysh V. I., Kalenskii S. V., Otrupcek R., Voronkov M. A., 1999, MNRAS, 310, 1077
Walsh A. J., Burton M. G., Hyland A. R., Robinson G., 1998, MNRAS, 301, 640
Yorke H. W., Sonnhalter C., 2002, ApJ, 569, 846

This paper has been typeset from a TEX/LATEX file prepared by the author.